Research article

Impact of trivalent Yttrium on the structural and optical properties of CaAl$_2$O$_4$: New frontier in supercapacitor positive electrode

E. Nkuna [a], M.R. Mhlongo [a], C. Dlamini [a,b], L.T. Melato [b], A. Bele [a,*], V. M. Maphiri [a,**]

[a] Department of Physics, Sefako Makgatho Health Sciences University, P. O. Box 94, Medunsa, 0204, South Africa
[b] Department of Applied Physical Sciences, Vaal University of Technology, Andries Potgieter Blvd, Vanderbijlpark, 1900, South Africa

ARTICLE INFO

ABSTRACT

In this work, trivalent Yttrium doped calcium aluminate (CaAl$_2$O$_4$:x% Y^{3+}) were synthesized for the first time. Through Photoluminescence (PL) spectroscopy and Commission Internationale de l'Eclairage (CIE), CaAl$_2$O$_4$:0.1 % Y^{3+} has demonstrated to be a potential high emitting phosphor material amongst other high concentration Y^{3+} doped samples, emitting a vibrant blue – pink hue where others are emitting a transiting hue from blue to green within a white vertex region. FTIR and UV–Vis have confirmed the prepared material and the presence of Y dopant. The SEM showed insignificant morphological change and the presence of pores, which were quantified using BJH and DFT methods to be micro – and meso–pores. Moreover, CaAl$_2$O$_4$ is also being reported as a positive electrode in supercapacitors for the first time. The analysis shows that it has superior performance within 1 M KOH electrolyte, with a specific capacity of 47.71 mA h g^{-1} at 1 A g^{-1} and a maximum power of 39.68 kW kg^{-1}. Trasatti's method showed a surface (138 Fg^{-1}) and diffusion (695 Fg^{-1}) contribution ratio of 17:83 (%) of the total stored energy. It has a capacity retention and columbic efficiency of 100 % at the end of 10 000 cycles, which was achieved via utilization of all micropores reaction sites. The EIS showed a small solution resistance of 0.75 Ω, indicating high ionic conductivity and a phase angle of – 50 °. Thus, these results show that CaAl$_2$O$_4$ is a potential candidate for photoluminescence and energy storage application.

1. Introduction

Over the years, there has been an increasing need for luminescent and energy storage materials for different purposes such as the development of mobile lighting electronics like electric vehicles and smartphones [1]. Extensive research has been conducted on aluminate phosphors due to their high efficiency, ability to emit long-lasting phosphorescence within a wide range of excitation wavelengths, mechanical strength, and chemical inertness [2]. These luminescent materials absorb energy and re-emit it as visible light, making them essential components in a wide range of lighting devices such as LED devices [3], and flat panel displays [4].

Calcium aluminate (CaAl$_2$O$_4$) also known as Krotite is a spinel with AB$_2$O$_4$ compound which belongs to the P21/n space group contains four formula units and exhibits a monoclinic structure. The lattice parameters for this structure are $a = 8.6996$, $b = 8.0994$, $c = 15.217$ Å, and $\beta = 90.188°$ [5]. This material has been previously synthesized using a variety of techniques such as solvothermal [6],

* Corresponding author.
** Corresponding author.
E-mail addresses: abongile.bele@gmail.com (A. Bele), vusanimuswamaphiri@gmail.com (V.M. Maphiri).

spray pyrolysis [7], combustion [8], co-precipitation [9], and citrate sol-gel [10,11]. The citrate sol-gel technique is relatively inexpensive, produces samples with high homogeneity, manages stoichiometry better, and low – temperature synthesis [12]. Mabelane et al. [13] and Dlamini et al. [14] have successfully fabricated $CaAl_2O_4$ aluminate phosphor via the citrate sol-gel technique. $CaAl_2O_4$ showed the presence of various excitation and emissions peaks within the range of 200–300 and 400–800 nm, respectively, due to the defects within the material matrix [13,14]. This material has been doped at various degrees using rare earth ions (RE^{3+}) to improve the luminescent characteristics of nanomaterials [15]. Dlamini et al. [14] have reported co-doped $CaAl_2O_4$ with 0.1 % Tb^{3+}; x% Sm^{3+}. The Photoluminescence (PL) results illustrated multiple emission peaks at 420, 440, 484, 548, 558, 562, 584, 603, and 654 nm attributed to defects within $CaAl_2O_4$ material and Tb^{3+} - Sm^{3+} emission transitions. Yttrium (Y) ions have been reported to widen the band gap of semiconductors such as ZnO [16], leading to a substantial enhancement in the optical properties, photocatalytic efficiency and stability. It has also been reported to have the ability to enhance the emission wavelength and enable the creation of an extremely responsive UV detector [17]. Viswanath et al. [18] conducted a study on the characterization, optical absorption, and photoluminescence of ZnS: Y^{3+}. The PL results revealed that the introduction of Y^{3+} doping in ZnS has led to the complete suppression of blue emission, while three distinct emission peaks at 363 nm, 469 nm, and 601 nm have emerged as a result of the 5d and 4f transitions within Y^{3+} ions. PL spectra analysis also reveals that with increasing Y^{3+} concentration, the emission peaks exhibit a slight shift towards the higher wavelengths, attributed to the introduction of newly occupied states by Y^{3+} 4f electrons, which reside within the band gap of ZnS. The introduction of Y^{3+} led to lattice distortion, subsequently influencing the energy levels of defect states in ZnS.

Various spinels such as $NiFe_2O_4$ [19], $NiCo_2O_4$ [20,21], Mn_2O_4 [22] and Fe_3O_4 [22] have been used as an electroactive material for energy storage such as batteries and supercapacitors. Although metal oxide including spinel suffers from low conductivity, it has shown high specific capacity and high electrode stability [23–25]. Adewinbi et al. [26] showed a higher area capacity (25.78 mAh cm^{-2}) and electrode stability of 84.4 % on the Co@MnO_2 film electrode. $CaAl_2O_4$ has not been reported as an electroactive material for supercapacitor application. Only Al–based compounds such as MIL – 53(Al) [27], Mg–Al LDH [28] and Al-doped Co_xP@graphene [29] composite has been reported as an electroactive material for supercapacitor application. Xu et al. [27] prepared MIL-53(Al) using the solvothermal method where polyethylene terephthalate (PET) bottle waste and aluminium cans were placed into a Teflon – lined stainless steel autoclave and submerged into a high temperature of 180 $°C$. The electrochemical results showed a higher specific capacitance of 355 F g^{-1} at 0.5 A g^{-1} in a three-electrode configuration and a high energy density of 20.1 Wh kg^{-1} at a power density of 225 W kg^{-1} [27]. Remesh et al. [28] prepared Mg–Al LDH (layered double hydroxide) infused into laser-scribed graphene for supercapacitor applications and the results showed an area capacitance and energy density, measuring 40 mFcm^{-2} and 0.00296 mWhcm^{-2}, respectively, at a current density of 0.08 mAcm^{-2}. The fabricated microsupercapacitor has exceptional bending capabilities and capacitance retention of 89.2 % after 5000 cycles. Moreover, induction of Mg–Al LDH pseudocapacitance material improved the overall effectiveness of the oil palm lignin-derived graphene electrode [28]. Lastly, Al-doped Co_xP@graphene showed a specific capacity of 312.3 mAhg^{-1} at a current density of 1 Ag^{-1} and capacitance retention of 87 % (at 40 Ag^{-1}).

Here in, we report the preparation of $CaAl_2O_4$ doped Y^{3+} for photoluminescence and using $CaAl_2O_4$ as a positive electrode for supercapacitor energy storage application. Thus, the primary objective of our study is to conduct a comprehensive investigation on $CaAl_2O_4$ doped Y^{3+} with an aim to gain better understanding of the material properties for the ultimate goal of developing more advanced nanophosphor material for applications such as LED. Furthermore, our work also shows the possibility of using $CaAl_2O_4$ as a high-energy and stable Ca–Al–based compound. This compound is the simplest to prepare among the Al-based literature [27–29], and it has a maximum total capacitance of 833 F g^{-1}, where diffusion and surface have contributed 695 and 138 Fg^{-1} respectively according to Trasatti's method. It also has a maximum power of 39.68 kW kg^{-1} estimated from the solution resistance from the EIS. Lastly, our work sheds light, schematical, behind the reason capacity or capacitance increases during stability, and also the decrease in rate capability.

2. Experimental

2.1. Material and electrode preparation

The citrate sol-gel technique was employed to synthesize the $CaAl_2O_4$ phosphor [10,30,31]. Appropriate mass of calcium nitrate tetra-hydrate Ca(NO₃)₂•4H₂O (98 %), aluminium nitrates nano-hydrate Al(NO₃)₃•9H₂O (98 %) and citric acid C₈H₈O₇•H₂O (99 %)
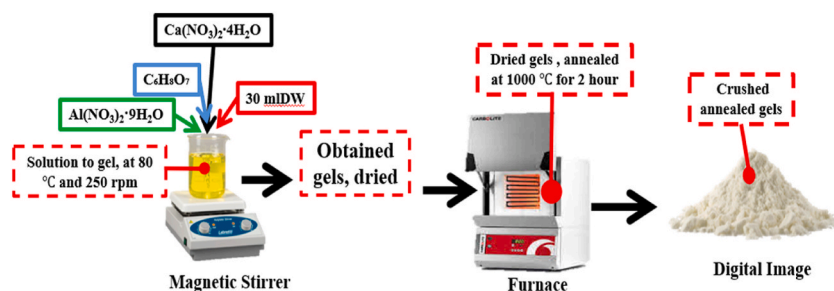
Fig. 1. The proposed citrate sol-gel synthesis mechanism.

were dissolved in a beaker filled with deionized water (DW). The stoichiometric molar ratios of Ca: Al and Ca: CA were kept at 1:2 and 1:0.75, respectively. To dope $CaAl_2O_4$ with different x mol% Y^{3+} ($0 \leq x \leq 2$) concentration $Y(NO_3)_3 \bullet 6H_2O$ (99 %) were added in a beaker at a specified amount (corresponding to the expected Y^{3+} dopant concertation) together with the above–mentioned $CaAl_2O_4$ precursors. The solution was stirred using a magnetic stirrer at a constant temperature of ~80 °C until a gel was formed. The obtained gel was placed in a glass Petri dish and allowed to dry at room temperature (RT) for 2 h followed by annealing in a muffle furnace at a temperature of 1000 °C for 2 h. The obtained white powder was crushed using a mortar and pestle and stored for analysis. Note that, the synthesis schematic is displayed in Fig. 1.

The positive electrode was prepared using the 80:10:10 ratio of electroactive $CaAl_2O_4$ prepared material, acetylene carbon black and polyvinylidene difluoride with a few drops of ethanol. This slurry was pasted onto 1.0×1.0 cm^2–1.6 mm (area – thickness) Nickel foam current collector. The as-prepared electrodes were subsequently dried at 60 °C in an electric oven for 8 h, then taken for electrochemical analysis. The prepared electrode had a mass loading of approximately 2.1 mg.

2.2. Characterization

The Bruker D2 Benchtop diffractometer with a CuKα of 1.5405 Å Powder X-ray diffraction (XRD) was used to analyze the crystalline structure of the prepared samples. The Nicolet iS50 Fourier Transform Infrared (FT-IR) spectrometer was employed to analyze the vibration bands of the $CaAl_2O_4$ structure. The Zeiss Supra 55 scanning electron microscope (SEM) coupled with Oxford energy dispersive X-ray spectrophotometry (EDS) detector was used to examine the surface morphology together with elemental composition and its distribution. Cary 500 scan UV–Vis–NIR spectrophotometer system was utilized to study the absorption and band gap of the prepared samples. The RT photoluminescence was carried out using Edinburgh instrument FS5 spectrofluorometer using a xenon lamp as an excitation source. The N_2 sorption isotherms of the prepared samples were measured at 77 K from 0.01 to 1.0 relative pressure (P/Po) using a Micrometrics TriStar II 3020 pore analyzer. The active surface area was determined using Brunauer – Emmett - Teller (BET), Density functional theory (DFT) and Barrett – Joyner - Halenda (BJH) method was used to describe the pore size distribution. Three electrode configurations measurements: cyclic voltammeter (CV), galvanostatic charge-discharge (GCD) and electrochemical impendence spectroscopy (EIS) of the $CaAl_2O_4$ positive electrode were performed using the Biologic VMP-3 Knoxville TN 37 930, USA potentiostat controlled using EC–Lab software, with the prepared electrode, Ag/AgCl and glassy carbon as a working, reference and counter electrode, respectively.

3. Results and discussion

3.1. X-ray diffraction

XRD analysis was performed to examine the crystal structure of $CaAl_2O_4$:x% Y^{3+} ($0 \leq x \leq 2.0$) powder samples as displayed in Fig. 2. Note that the $CaAl_2O_4$ (undoped) is designated as the host. The XRD peaks are sharp and well-defined indicating high crystallinity, and their diffraction patterns exhibited an excellent match with the standard pattern of monoclinic $CaAl_2O_4$ spinel (JCPDS No. 70–0134) with the lattice constants a = 8.702 Å, b = 8.092 Å and c = 15.18 Å [5]. There were no observable traces of impurities such as CaO, Al_2O_3, or any related Y–based compounds in all the prepared samples. These patterns show that the crystal structure of $CaAl_2O_4$ was not altered even when varying Y^{3+} concentration due to the relatively low concentration of the dopant. Further suggesting a successful Y^{3+} ion incorporation within the $CaAl_2O_4$ matrix [32]. Several studies such as Mabelane et al. [33], Dlamini et al. [34] and Shashikala et al. [35], have shown similar results. The crystallite sizes (*D*) together with induced strain (ε) of the prepared samples were analysed using the below Williamson – Hall on Eq. (1) [36]:
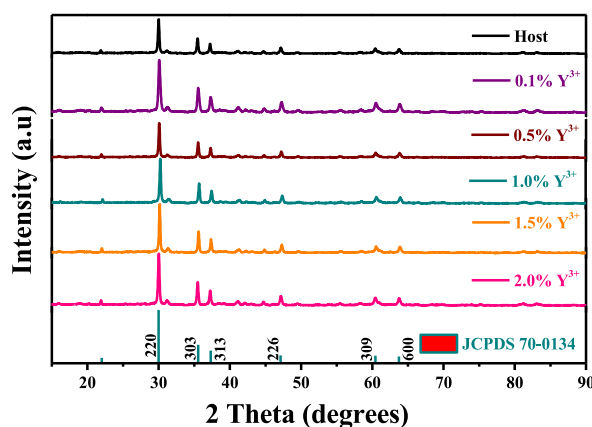
Fig. 2. The XRD patterns for $CaAl_2O_4$:x mol% Y^{3+} ($0 \leq x \leq 2.0$).

$$\beta \cos \theta = \frac{k\lambda}{D} + 4\varepsilon \sin \theta \tag{1}$$

Where β represents the full width at half maximum (FWHM) intensity of the diffraction peak in rads, θ is the diffraction peak center in rads, k is a constant value of 0.94, and λ represents the wavelength of the incident X-rays of 1.5405 Å. The obtained Williamson–Hall diagrams for all the samples are displayed in Fig. S1 (supplementary information), strain and crystallite size are displayed in Table 1.

The most prominent peak (220) was used for further XRD diffraction analysis. The analysis of the (220) peak of the prepared samples is displayed in Fig. 3 (a) whereas the peak centres versus x% Y^{3+} are displayed in Fig. 3 (b). There is a peak shift towards the high diffraction angle compared to $CaAl_2O_4$, suggesting a decrease in the lattice parameter (lattice spacing) of the doped samples. This behaviour can be attributed to the replacement of bigger ionic radius Ca^{2+} ions (1.12 Å) [36] with a smaller ionic radius Y^{3+} (1.04 Å) [37] or Al^{3+} (0.95 Å) [37] as shown in Fig. 3 (c). The only substitution that led to the shrinking of the Ca–Al radii is the replacement of Ca by Y. Fig. 3 (d) shows a general trend of the decrease of FHWM and an increase of crystallite size suggesting that low concertation is destructive as compared to higher concentration since higher dopant concentration ions are more likely to form arrays of their own. Fig. 3 (e) and (f) show a structural schematic diagram of $CaAl_2O_4$ and doped $CaAl_2O_4$: Y^{3+} where the undoped sample has minimum defects leading to a lower diffraction angle and FWHM suggesting that the material is more crystalline as can be seen on Fig. 3 (a), (b) and (d), the doped sample (Fig. 3 (f)) shows the opposite.

3.2. Scanning electron microscopy

The surface morphology of the selected nanopowder samples were investigated using the SEM technique, and the results are illustrated in Fig. 4. The morphology of the $CaAl_2O_4$ in Fig. 4 (a) reveals the presence of small irregular aggregates scattered on the surface with different sizes, together with pores of different sizes which might have occurred during the extermination of water and other gases during the annealing process. The morphology on Fig. 4 (b)–(d) is similar to that of the undoped material, with that of 0.1 % Y^{3+} showing fewer particle agglomeration. In general, such morphology is suitable for supercapacitor energy storage applications where different pores observed serve as active centres (micropores), pathways (mesopores) and reservoirs (macropores) for the electrolyte. The $CaAl_2O_4$ was further subjected to BET, BJH and DFT methods to understand the surface area, type and population of the available pores.

3.3. Energy dispersive spectroscopy

Fig. 5 illustrates the EDS spectra of (a) $CaAl_2O_4$ and (b) 2.0 % Y^{3+} samples. The results confirm the anticipated existence of elements Ca, Al, O and Y. The appearance of a carbon (C) peak can be attributed to the utilization of carbon tape for sample mounting during the EDS measurement preparation. These figures show that there were no observable traces of impurities. Fig. 5 (c) and (d) illustrate the elemental mapping of the $CaAl_2O_4$ and 2.0 % Y^{3+}, revealing a uniform distribution of Ca, Al, O, and Y across the surface.

3.4. Fourier-transform infrared spectroscopy, ultra-violet visible spectroscopy and photoluminescence analysis

Fig. 6 (a) displays the FTIR spectra of the $CaAl_2O_4$:x% Y^{3+} ($0 \leq x \leq 2.0$) and the spectra were recorded to analyze the vibrational frequencies and identify the functional groups present in the prepared nanopowder samples. The prominent bands observed at 629 cm^{-1} and 780 cm^{-1} are likely associated with the vibrational modes of AlO_6 and AlO_4 [38]. The two robust bands at 1219 cm^{-1} and 1370 cm^{-1}, along with the sharp peak at 1737 cm^{-1}, can be attributed to the presence of the doping ions [39], as they were not observed on the host sample.

UV–Vis diffuse reflection spectroscopy was employed to examine the distinctive absorption properties of the $CaAl_2O_4$:x% Y^{3+} ($0 \leq x \leq 2.0$) series and the observed spectra are displayed in Fig. 6 (b). It can be observed that the absorption spectra showed multiple peaks at different wavelengths located at 264, 424, 603 and 640 nm. The absorption peak at 264 nm, which can be attributed to the $O^{2-} \rightarrow Al^{3+}$ charge transition is due to the excitation of electrons from the valence band gap of oxygen (2p) to the conduction band of aluminium (3d) [40]. This is consistent with the previously reported peak at 240 nm for pure $CaAl_2O_4$ by Mabelane et al. [33]. The 424 nm notch can be attributed to the transition from the $^4f_{12} \rightarrow ^5d_1$ state of the Y^{3+} ions [41], while the notches at 603 and 640 nm are due to the instrument. These results together with the FTIR and EDS showed the presences of Y ions within the $CaAl_2O_4$ host matrix.

Fig. 6 (c) presents the room temperature PL excitation and emission spectra of $CaAl_2O_4$: x% Y^{3+} ($0 \leq x \leq 2.0$) samples. Fig. 6 (d) illustrates the normalized emission spectra. The excitation spectra were recorded while monitoring the emission at 550 nm, the results

Table 1
Sample identification, crystallite size, strain, centre (2 Theta), and FWHM of peak (220).

Parameters	$CaAl_2O_4$:x% Y^{3+}					
	Host	0.1 % Y^{3+}	0.5 % Y^{3+}	1.0 % Y^{3+}	1.5 % Y^{3+}	2.0 % Y^{3+}
Crystallites Size (nm)	42.13	30.06	41.87	37.22	42.49	58.05
Strain ($\times 10^{-3}$)	2.809	2.605	2.660	2.604	2.583	2.741
2 Theta (degree)	29.93	30.09	30.07	30.23	30.15	30.03
FWHM($\times 10^{-1}$)	1.953	2.736	1.965	2.211	1.936	1.417
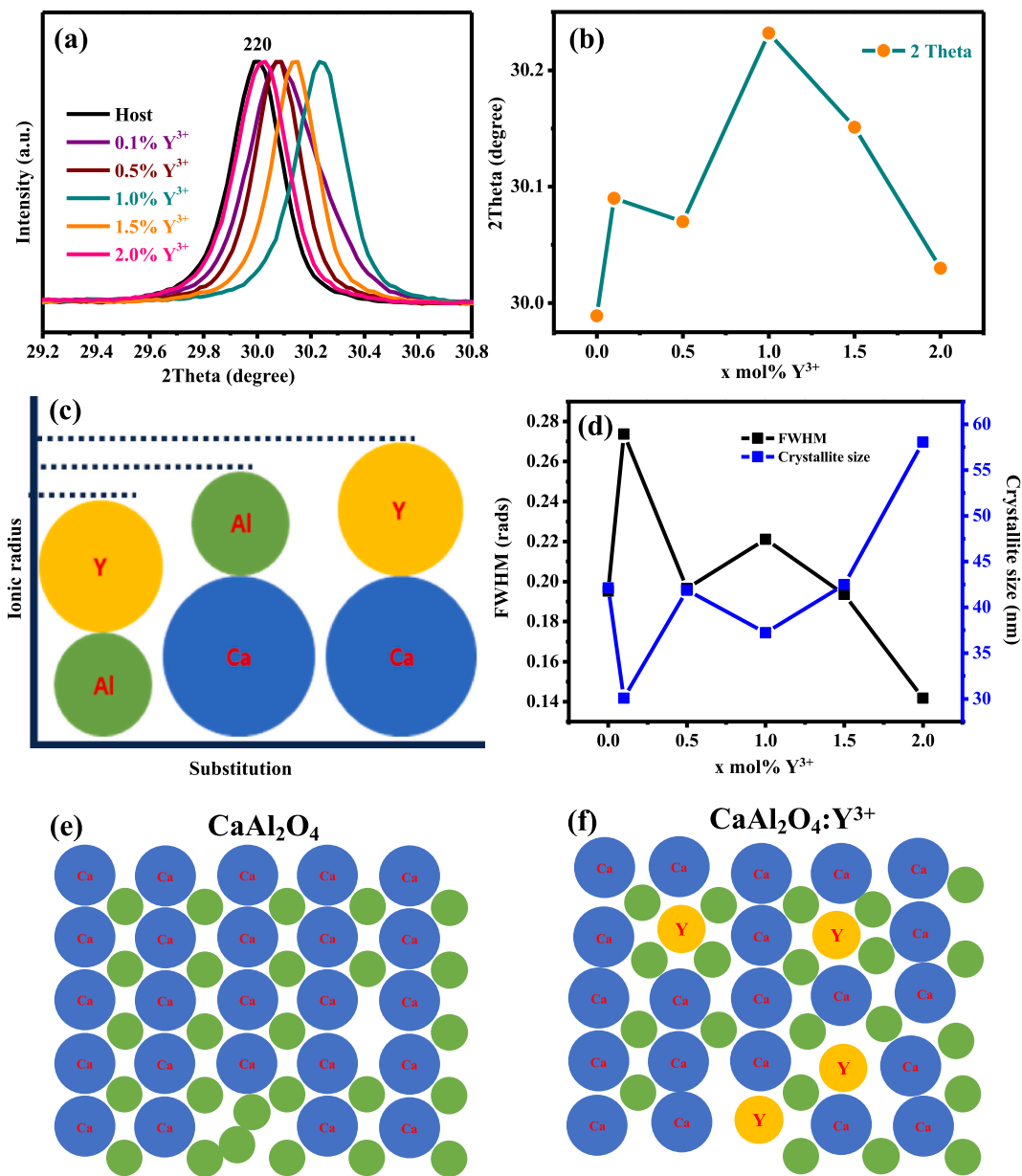
Fig. 3. (a) Analysis of the (220) diffraction peak, (b) 2 Theta versus x mol% Y^{3+}, (c) ionic radius versus substitution, (d) FWHM and crystallite size versus x mol % Y^{3+}, and (e) and (f) schematic of $CaAl_2O_4$ and $CaAl_2O_4$: Y^{3+}.

show the existence of two distinct excitation peaks located at around 213 nm and 273 nm, respectively. The excitation peak observed at 213 nm can be ascribed to the band-to-band gap of $CaAl_2O_4$ [42]. The peak at 273 nm could be a result of imperfections within the host material, as there were no shifts in excitation peak observed for the Y^{3+} doped samples. The emission monitored under the 213 nm excitation wavelength showed the presence of three peaks at 446, 550, and 674 nm which can be attributed to the host material [13, 14]. The 273 nm excitation peak, and 446 and 550 nm emission peak intensity as a function of x mol % Y^{3+} are displayed in Fig. 6 (e). It can be seen that the 0.1 % Y^{3+} has the highest emission intensity, this behaviour can be attributed to the increased defects with the $CaAl_2O_4$ matrix. This defect introduces variations within the crystal structure, leading to the broadening of XRD peaks (larger FWHM). The broadening is often associated with reduced crystallite size or increased lattice disorder [42]. The presence of dislocations in the crystal lattice, as observed in XRD, may introduce localized energy levels impacting the radiative recombination of electron-hole pairs, affecting the intensity and spectral characteristics of PL observed in the material [43]. The observed emission spectra were further analysed for their emission colour which is displayed in Fig. 6 (f) and the CIE coordinates are on Table 2. This was accomplished using CIE coordinate calculator software [10]. The CIE diagram showed that varying concentrations of Y^{3+} influence the emission colour of the prepared nanophosphor, the 0.1 % Y^{3+} sample has shown to emit a vibrant blue–pink hue whereas others were emitting a transiting
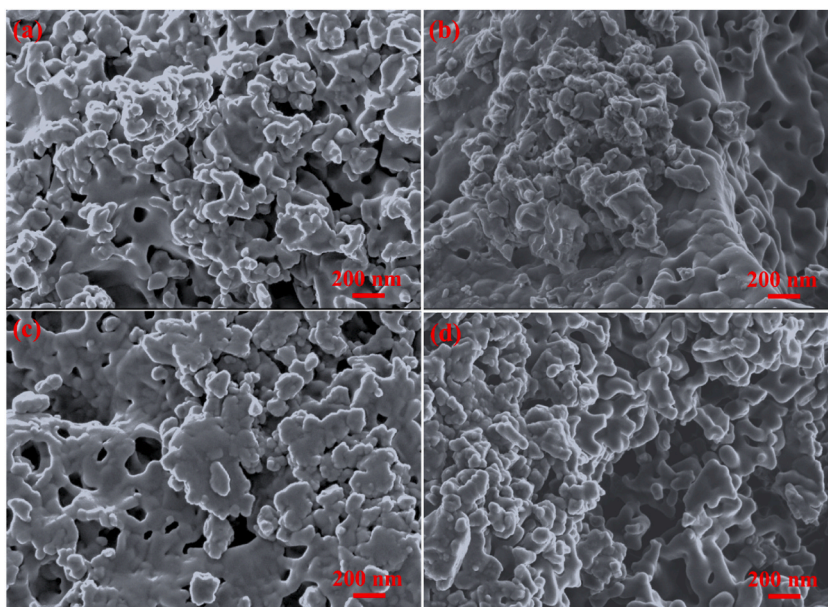
Fig. 4. SEM images for (a) CaAl$_2$O$_4$, (b) 0.1 % Y^{3+}, (c) 0.5 % Y^{3+} and 2.0 % Y^{3+}.

hue from blue to green within a white vertex region.

The colour purity was calculated from Eq. (2) [43].

$$\text{Colour purity} = \frac{\sqrt{(x - x_i)^2 + (y - y_i)^2}}{\sqrt{(x_d - x_i)^2 + (y_d - y_i)^2}} \times 100 \qquad (2)$$

where, x, y represents the chromaticity coordinate of CaAl$_2$O$_4$:x% Y^{3+}, which in this case are (0.2637, y = 0.3158). The coordinates of the illuminate point are denoted as x$_i$, y$_i$ (x$_i$ = 0.333, y$_i$ = 0.333). Additionally, x$_d$ and x$_d$ represent the coordinates of the dominant emission wavelength (x$_d$ = 0.2977, y$_d$ = 0.1624). The correlated colour temperature (CCT) of the synthesized phosphors is determined using McCamy's empirical Eq. (3) expressed as follows [44]:

$$CCT = -449n^3 + 3525n^2 - 6823n + 5520.33 \qquad (3)$$

Here, the formula n $= \frac{x - x_e}{y - y_e}$ is used to calculate the value of n based on the chromaticity coordinate (x, y) and a reference point (x$_e$, y$_e$), where (x$_e$ = 0.332, y$_e$ = 0.186) which is the epicentre.

3.5. Textural and electrochemical analysis

Fig. S2 displays nitrogen adsorption-desorption plots (isotherms) for the CaAl$_2$O$_4$ sample, along with its corresponding pore size distribution, cumulative pore volume and cumulative surface area distribution, as per the BET and DFT method. The isotherm curves illustrated on Fig. S2 (a) exhibited characteristics of a Type IV isotherm with H3 hysteresis loop behaviour, as per the IUPAC classification [45], exhibiting a BET surface of 3 m^{2}g^{-1} and an average pore diameter of 4.25 nm. Fig. S2 (b) shows a pore size (diameter) distribution with the presence of micro-and meso–pore further suggesting that CaAl$_2$O$_4$ is suitable for supercapacitor application as suggested from the SEM images displayed in Fig. 4. BJH was used to quantify the ratio of micro–meso–pore ratio, where the micropore volume is calculated to be 2 m^{2}g^{-1} and total pore volume is 3 m^{2}g^{-1}. Thus, the micro–memo–pore ratio is 66 %–33 % (1 m^{2}g^{-1}) which is a good balance pore ratio. It contains 66 % of micropore suggesting enough reaction surface area and 33 % of mesopore also suggesting enough ion passage into the micropore reaction surface area. Fig. S2 (c) and (d) show that cumulative pore volume and surface area as a function of pore size distribution, it is clear the mesopore increases the total pore volumes (4 × 10^{-3} ccg^{-1}). However, it doesn't significantly increase the total surface area (3 m^{2}g^{-1}).

The electrochemical performance of the CaAl$_2$O$_4$ was evaluated in the three-electrode configuration in the positive potential window using three different electrolytes at a scan rate of 20 mV s^{-1} as shown in Fig. 7 (a). The 1 M KOH electrolyte showed a higher current response, which is a better performance compared to 1 M NaOH and 1 M Li$_2$SO$_4$ electrolytes due to the ionic conductivity of OH$^-$ anions within the 1 M KOH electrolyte [46,47]. The GCD curve in Fig. 7 (b) shows that the 1 M KOH has the best electrochemical performance among other electrolytes and it allowed GCD to reach a higher potential window of 0.5 V. The 1 M KOH electrolyte was used for electrochemical analysis throughout this study because it has shown much better electrochemical results as compared to the
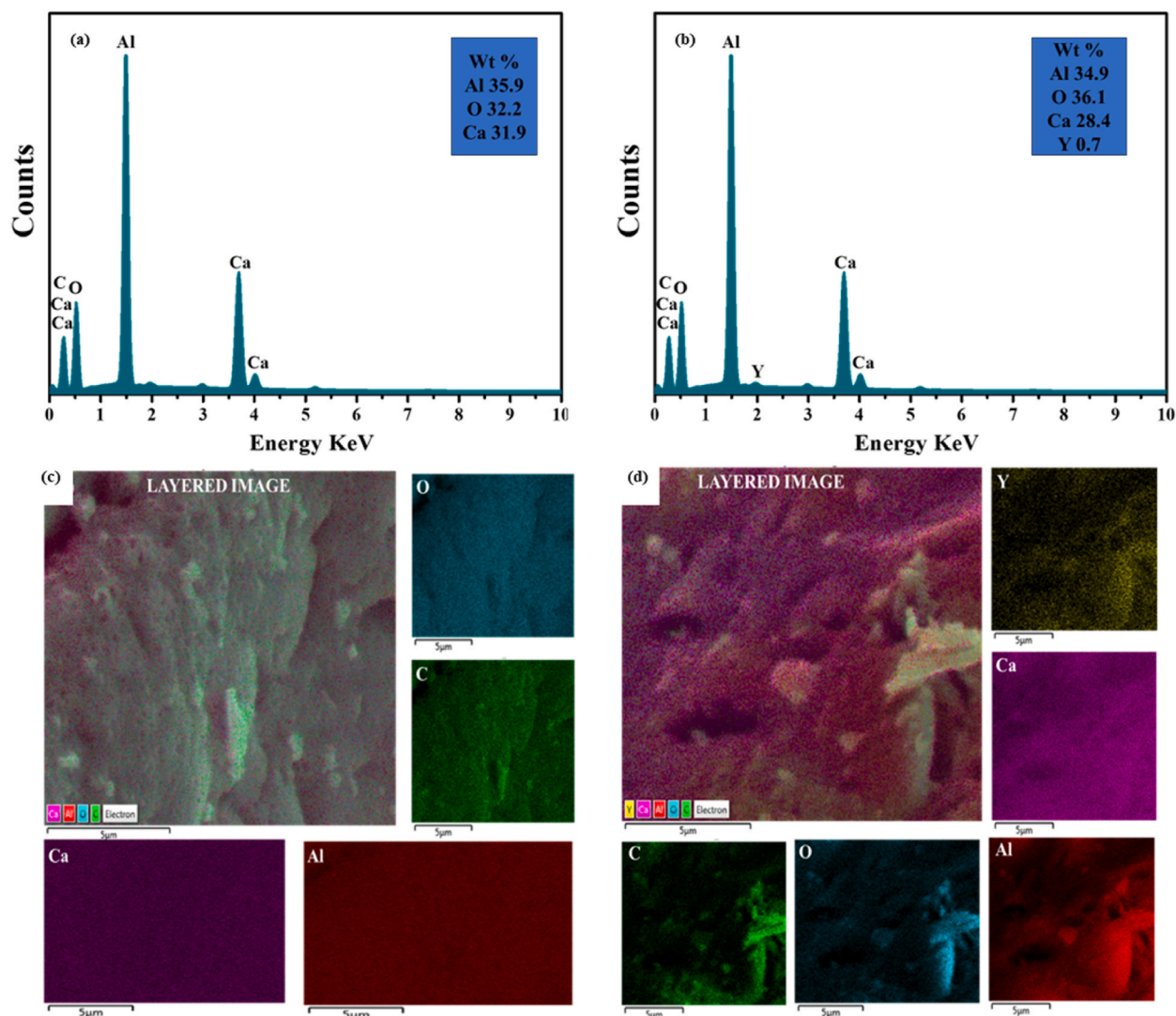
Fig. 5. The EDS spectrum and maps of (a, c) host and (b, d) $CaAl_2O_4$:2.0 % Y^{3+}, respectively.

other electrolytes on the $CaAl_2O_4$ electrode material. The CV curves displayed in Fig. 7 (a) are showing some faradaic behaviour due to the interaction between the 1 M KOH electrolyte and the $CaAl_2O_4$. This was also observed on the GCD curve displayed in Fig. 7 (b). The specific capacity (Q_s) of the $CaAl_2O_4$ was calculated from the GCD curve in Fig. 7 (b) using Eq. (4) below [48,49].

$$Q_s = \frac{I_s \times t}{3.6} \left[mA\ hg^{-1} \right]$$

(4)

where I_s, m and t are specific current (mA), mass (mg) and discharge time (s), respectively. The obtained specific capacity of 1 M KOH, 1 M NaOH and 1 M Li_2SO_4 were 47.08, 42.95 and 41.49 mA h g^{-1}, respectively at 2 Ag^{-1}. It can be seen that 1 M KOH has higher specific capacity. The electrical properties of the $CaAl_2O_4$ were analysed using EIS, as shown by Nyquist plot displayed in Fig. 7 (c) and (d). It determines the nature of the active material on the electrode/electrolyte interface. This Nyquist plot lacks a higher region frequency semi-circle suggesting a low electrode/electrolyte interface charge transfer resistance suggesting a better capacitive behaviour [50]. The real impedance (Re Z) axis intercept in the high-frequency region indicates the equivalent series resistance or solution resistance (R_s) that describes the interfacial contact resistance between the active materials and NF current collector, electrode/electrolyte interface and the internal resistance of the electroactive material [50,51]. The R_s values for 1 M KOH, 1 M NaOH and 1 M Li_2SO_4 are 0.75, 2.69 and 2.62 Ω, respectively indicating the 1 M KOH has a lower resistance or more electrical conducting capacity. The maximum power, P_{max} of $CaAl_2O_4$ within the 1 M KOH electrolyte was estimated from Eq. (5) below to be 39.68 kW kg^{-1}

$$P_{max} = \frac{\Delta V^2}{4m(R_s)}$$

(5)
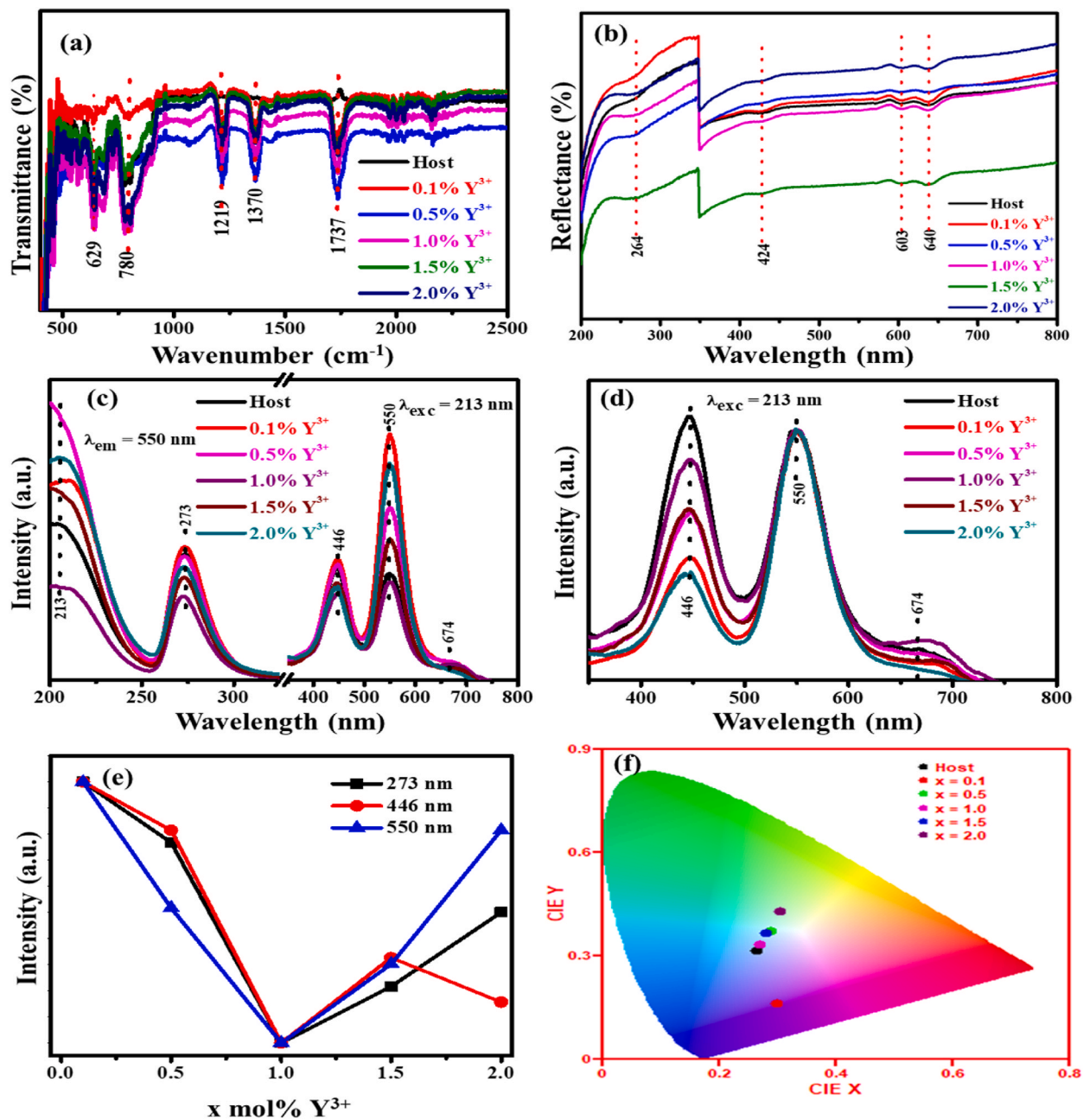
Fig. 6. (a) FTIR and (b) diffuse reflectance spectra. (c) Emission and excitation spectra, (d) normalized emission spectra, (e) intensity as a function x mol% Y^{3+} and (f) CIE diagram of the $CaAl_2O_4$: x% Y^{3+} ($0 \leq x \leq 2.0$).

Table 2
Summary of sample identification, CIE coordinate, colour purity and CCT.

Sample ID	CIE coordinate (x; y)	Colour purity (%)	CCT (K)
Host	(0.2637; 0.3158)	40.99	1025
0.1 % Y^{3+}	(0.2977; 0.1624)	97.02	6627
0.5 % Y^{3+}	(0.2874; 0.3715)	34.26	7341
1.0 % Y^{3+}	(0.2702; 0.3339)	36.05	9025
1.5 % Y^{3+}	(0.2797; 0.3662)	36.04	7778
0.1 % Y^{3+}	(0.3026; 0.4286)	57.58	–
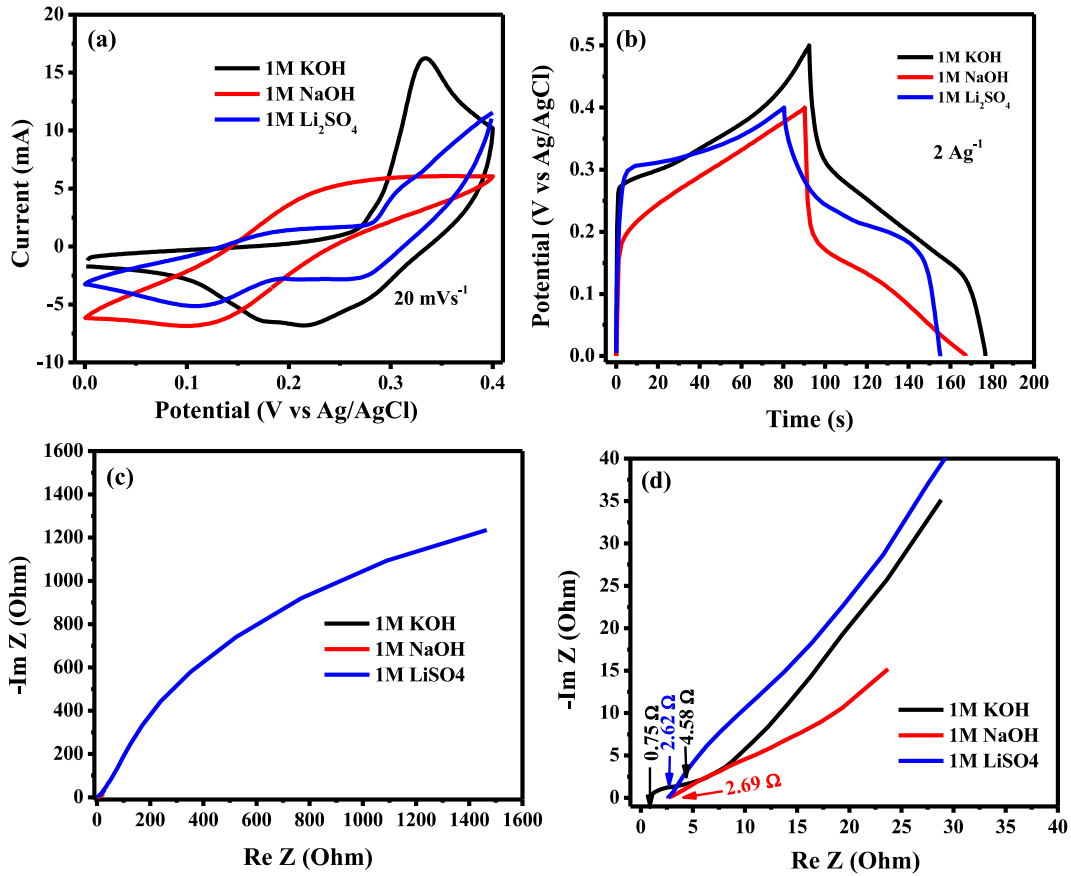
Fig. 7. (a) CV, (b) CD, and (c) and (d) Nyquist plot of $CaAl_2O_4$ at different electrolyte.

where ΔV, m and R_s are the cell potential (V), electrode mass of 2.1×10^{-6} kg and R_s of 0.75 Ω determined from the Nyquist plot in Fig. 7 (d), respectively.

The CV curves of the $CaAl_2O_4$ at different scan rates are displayed in Fig. 8 (a). The CV curves of the device are asymmetric in shape, slightly distorted rectangular-like shape indicating electric double layer capacitor (EDLC) behaviour which is constant throughout the various scan rates, suggesting a good charge propagation and fast ionic transport [52]. The GCD curve obtained at various specific currents displayed in Fig. 8 (b) shows faradaic behaviour throughout the different specific currents agreeing with the CV curves in Fig. 8 (a) confirming the good capacitive behaviour. The specific capacity as a function of specific current is displayed in Fig. 8 (c) and was calculated using Eq. (4) showing a maximum specific capacity of 47.71 mA h g^{-1} at 1 A g^{-1} and a reduction to 14.85 mA h g^{-1} at 10 A g^{-1} which can be attributed to the limited time that ions have to interact with the surface of the electrode [47,53].

Trasatti analysis [54] (Fig. S3) was performed to calculate the diffusion–surface contribution capacitance also displayed in Fig. 8 (d). Maximum total capacitance (C_T) was obtained from the reciprocal of the extrapolated intercept of the $1/C_T$ versus $v^{0.5}$ and maximum surface contribution (C_{dl}) was estimated by extrapolating intercept of C_{dl} versus $v^{-0.5}$, while maximum diffusion contribution (C_d) was obtained from the difference between total and surface contribution (Eq. (S1)). The obtained values are displayed in Table S1 and Fig. 8 (d). It is observed that the diffusion contribution accounts for 83 % of the stored energy while the surface contribution holds 17 %, hence, the CV and CD curve displayed in Fig. 8 (a) and (b) shows faradaic behaviour. This is confirmed by the phase angle of $-50°$ displayed in Fig. 8 (e) which is not far from the ideal phase angle of $-90°$ [55] taking note that this is a faradaic material. The frequency dependent Real (Re C) and imaginary (Im C) capacitances are displayed in Fig. 8 (f) calculated from Eqs. (6)–(9) where the impedance $Z(\omega)$ with $\omega = 2\pi f$ is expressed as

$$Z(\omega) = \frac{1}{j\omega \times C(\omega)} \tag{6}$$

$$Re\ C = \frac{Z''(\omega)}{\omega |Z(\omega)|^2} \tag{7}$$
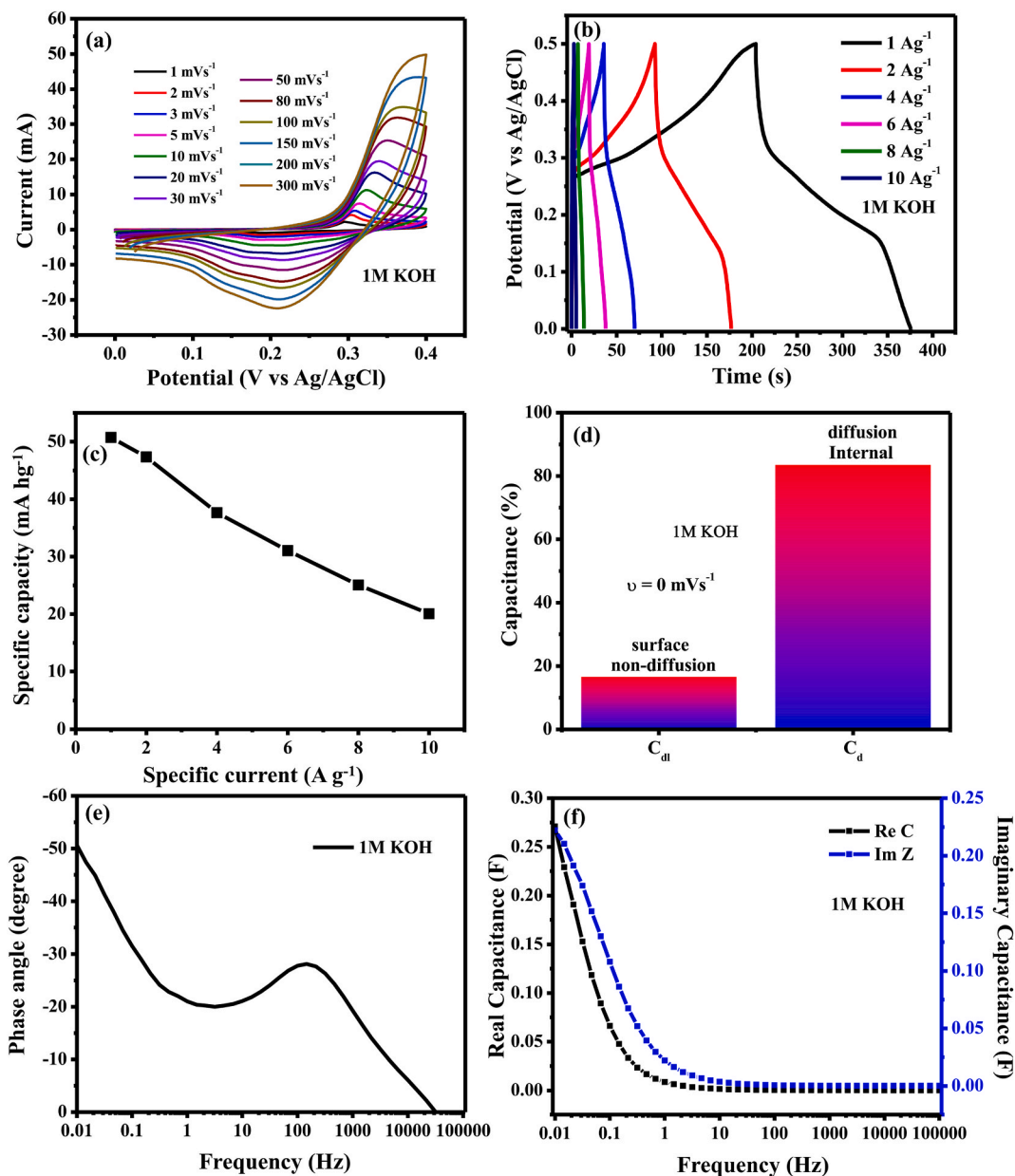
Fig. 8. (a) CV at different scan rates, (b) GD at different specific currents, (c) Specific capacity versus specific current, (d) surface and diffusion-based capacitance, (e) phase angle and (f) real and imaginary plot of capacitance as a function of frequency.

$$Im\ C = \frac{Z'(\omega)}{\omega |Z(\omega)|^2} \tag{8}$$

$$|Z(\omega)|^2 = Z'(\omega)^2 + Z''(\omega)^2 \tag{9}$$

Fig. 8 (f) shows that the Re C accessible capacitance of 0.275 F and Im C gives a relaxation time ($\tau = 1/2\pi f$, where f is the peak of the frequency) around 15.0 s suggesting that the $CaAl_2O_4$ can be charged quickly.

The capacitive retention (CR) and columbic efficiency (CE) are calculated using Eq. (S2) and (S3), respectively, and the obtained graph is displayed in Fig. 9 (a). The CR increased from 80 to 100 % within the first few 3000 cycles and then remained at 100 % throughout. The CD curve used to calculate the capacity at point A (100), point B (2 000), point C (3 000) and at the end of the stability (10 000) are displayed on the inset of Fig. 9 (a). The CE remained at 100 % throughout the entire measurement indicating good reversibility and stable electroactive materials. The increase in the capacity can allude to the intercalation of electrolytes within the micropores while measuring the consecutive CD at 6 Ag^{-1} within the 1 M KOH electrolyte. This behaviour is shown schematically in
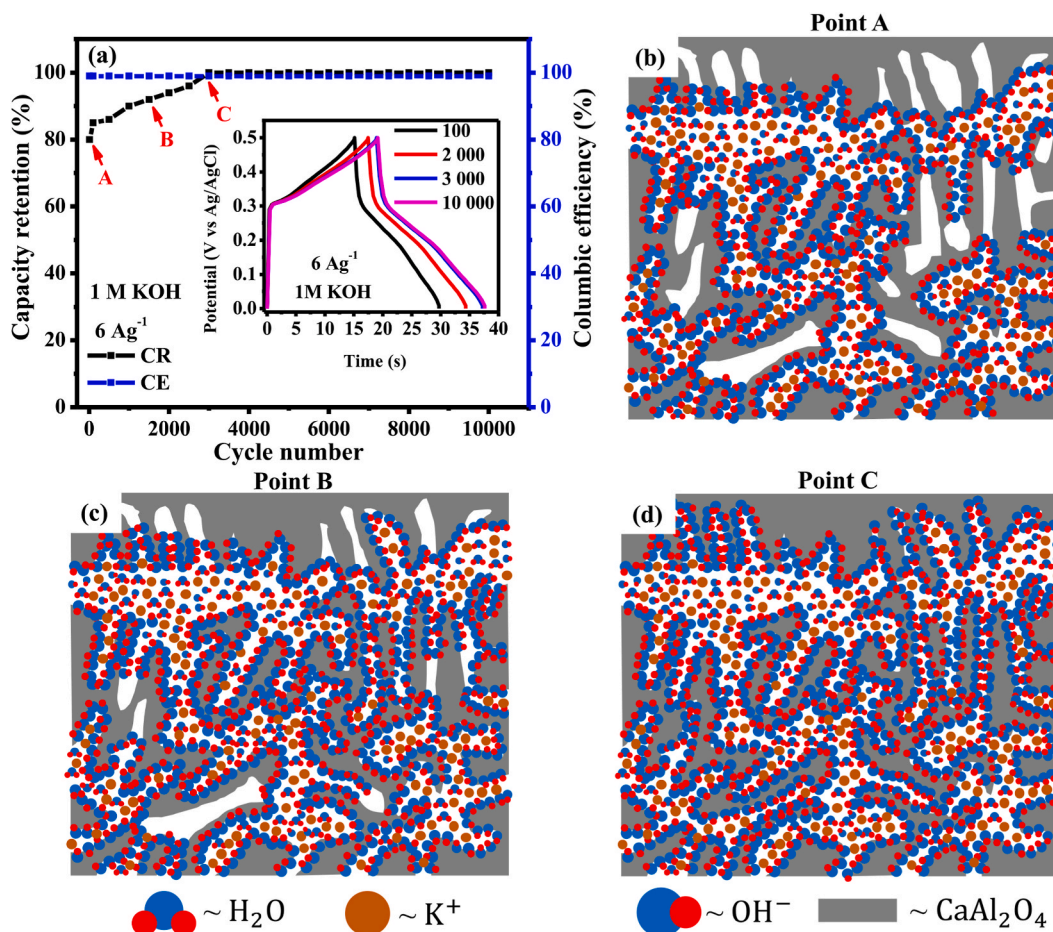
Fig. 9. (a) Capacity retention and columbic efficiency versus cycle number (inset: CD curve at 100 (point A), 2000 (point C), 3000 (point C) and 10 000 cycle number) and (b)–(d) movement of ions within the pores of CaAl$_2$O$_4$ during stability.

Fig. 9 (b)–(d), where some micropores are not utilized at point A leading to a capacity of 80 %, with continuation of CD to 2000 cycles. At point B more ions have intercalated more micropores compared to point A hence a capacity increase to 90 %. Then finally at point C (after 3000 cycles) almost all the micropores are utilized as the reaction centre of the CaAl$_2$O$_4$ material. Thus, 100 % capacity has been obtained. Our results suggest that the increase in capacity is due to the utilization of micropores since there is no change in the voltage (IR) drop suggesting that there is no electrode current collect corrosion or electroactive material reaction. In addition, the movement of ions (reaction time) is the reason for the fall of the rate capability in Fig. 8 (c), increasing the specific current reduces the time (see Eq. (4)). Thus, lesser ion reaches the micropores or react with the electroactive material.

4. Conclusion

In conclusion, the citrate sol-gel method has proven to be an effective synthesis method for trivalent Yttrium-doped calcium aluminate (CaAl$_2$O$_4$:x mol% Y^{3+}) nanopowder. The XRD analysis confirmed the single crystalline nature and monoclinic structure of all synthesized samples, with notable influences on the crystallographic parameters, this was further confirmed by the FTIR and UV–Vis. SEM revealed the morphology of the prepared samples, while EDS confirmed the expected elemental composition. Photoluminescence spectroscopy and CIE diagrams demonstrated that CaAl$_2$O$_4$: 0.1 % Y^{3+} exhibited a high emission potential, displaying a vibrant blue–pink hue, while the other samples display an emitting a transiting hue from blue to green within a white vertex region. In additional, the material's application as a positive electrode in supercapacitors was explored for the first time, showcasing superior performance in 1 M KOH electrolyte. The specific capacitance, maximum power, and cycling stability, phase angle and solution resistance of CaAl$_2$O$_4$ indicated its potential as a promising candidate for energy storage applications.

Data availability

Data will be made available on request.

CRediT authorship contribution statement

E. Nkuna: Writing – review & editing, Writing – original draft, Visualization, Validation, Formal analysis, Data curation, Conceptualization. **M.R. Mhlongo:** Writing – review & editing, Visualization, Supervision, Resources, Project administration, Methodology, Investigation, Funding acquisition, Formal analysis, Conceptualization. **C. Dlamini:** Writing – review & editing, Visualization, Validation, Methodology, Investigation, Formal analysis, Conceptualization. **L.T. Melato:** Writing – review & editing, Visualization, Validation, Resources, Investigation, Data curation, Conceptualization. **A. Bele:** Writing – review & editing, Writing – original draft, Visualization, Validation, Supervision, Software, Resources, Project administration, Methodology, Investigation, Funding acquisition, Formal analysis, Data curation, Conceptualization. **V.M. Maphiri:** Writing – review & editing, Writing – original draft, Visualization, Validation, Supervision, Software, Resources, Project administration, Methodology, Investigation, Funding acquisition, Formal analysis, Data curation.

Declaration of generative AI and AI-assisted technologies in the writing process

During the preparation of this work, the author(s) used Microsoft Bing to improve the readability of the content. After using this tool, the author(s) reviewed and edited the content as needed and took full responsibility for the content of the publication.

Declaration of competing interest

The authors declare the following financial interests/personal relationships which may be considered as potential competing interests:M.R. Mhlongo reports financial support was provided by National Research Foundation. If there are other authors, they declare that they have no known competing financial interests or personal relationships that could have appeared to influence the work reported in this paper.

Acknowledgements

Appendix A. Supplementary data

Supplementary data to this article can be found online at https://doi.org/10.1016/j.heliyon.2024.e33274.

References

[1] K. Murugesan, P. Sivakumar, P.N. Palanisamy, An Overview on Synthesis of Metal Oxide Nanoparticles, vol. 2, 2016, pp. 58–66.

[2] J. Kuang, Y. Liu, J. Zhang, White-light-emitting long-lasting phosphorescence in Dy3+-doped SrSiO3, J. Solid State Chem. 179 (2006) 266–269, https://doi.org/10.1016/j.jssc.2005.10.025.

[3] A.G. Bispo-Jr, L.F. Saraiva, S.A.M. Lima, A.M. Pires, M.R. Davolos, Recent prospects on phosphor-converted LEDs for lighting, displays, phototherapy, and indoor farming, J. Lumin. 237 (2021) 118167, https://doi.org/10.1016/j.jlumin.2021.118167.

[4] A.N. Yerpude, G.N. Nikhare, S.J. Dhoble, N.S. Kokode, Luminescence properties of rare earth Sm3+ and Tb3+ doped Ca3Al2O6 phosphor for solid state lighting, Mater. Today Proc. 15 (2019) 511–515, https://doi.org/10.1016/j.matpr.2019.04.115.

[5] R. Cao, F. Zhang, C. Cao, X. Yu, A. Liang, S. Guo, H. Xue, Synthesis and luminescence properties of CaAl2O4:Mn4+ phosphor, Opt. Mater. 38 (2014) 53–56, https://doi.org/10.1016/j.optmat.2014.10.002.

[6] W. Wang, S. Kunwar, J.Y. Huang, D.Z. Wang, Z.F. Ren, Low temperature solvothermal synthesis of multiwall carbon nanotubes, Nanotechnology 16 (2005) 21–23, https://doi.org/10.1088/0957-4484/16/1/005.

[7] J.H. Lee, J. Ryu, F.A. Jolesz, Z.H. Cho, S.S. Yoo, Brain-machine interface via real-time fMRI: preliminary study on thought-controlled robotic arm, Neurosci. Lett. 450 (2009) 1–6, https://doi.org/10.1016/j.neulet.2008.11.024.

[8] B.S. Barros, P.S. Melo, R.H.G.A. Kiminami, A.C.F.M. Costa, G.F. De Sá, S. Alves, Photophysical properties of Eu3+ and Tb3+-doped ZnAl2O4 phosphors obtained by combustion reaction, J. Mater. Sci. 41 (2006) 4744–4748, https://doi.org/10.1007/s10853-006-0035-6.

[9] V. Ciupina, I. Carazeanu, G. Prodan, Characterization of ZnAl2O4 nanocrystals prepared by coprecipitation and microemulsion techniques, J. Optoelectron. Adv. Mater. 6 (2004) 1317–1322.

[10] V.M. Maphiri, L.T. Melato, M.R. Mhlongo, T.T. Hlatshwayo, T.E. Motaung, L.F. Koao, S.V. Motloung, Effects of varying Alx moles on structure and luminescence properties of ZnAlxO1.5x+1:0.1 mol% Tb3+ nanophosphors prepared using citrate sol–gel method, J. Rare Earths 41 (2023) 358–364, https://doi.org/10.1016/j.jre.2022.04.026.

[11] V.M. Maphiri, B.F. Dejene, T.E. Motaung, T.T. Hlatshwayo, O.M. Ndwandwe, S.V. Motloung, The effects of varying the Eu3+ concentration on the structural and optical properties of Mg1.5Al2O4.5:x% Eu3+ (0 ≤ x ≤ 2) nanophosphors prepared by sol–gel method, Nanomater. Nanotechnol. 8 (2018), https://doi.org/10.1177/1847980418800644.

[12] S.V. Motloung, M. Tsega, F.B. Dejene, H.C. Swart, O.M. Ntwaeaborwa, L.F. Koao, T.E. Motaung, M.J. Hato, Effect of annealing temperature on structural and optical properties of ZnAl2O4:1.5% Pb2+ nanocrystals synthesized via sol-gel reaction, J. Alloys Compd. 677 (2016) 72–79, https://doi.org/10.1016/j.jallcom.2016.03.170.

[13] T.S. Mabelane, L.F. Koao, S.V. Motloung, T.E. Motaung, R.E. Kroon, M.R. Mhlongo, Effect of annealing period on the structure, morphology, and optical properties of CaAl2O4:0.1% Sm3+ prepared by citrate sol-gel method, J. Mol. Struct. 1260 (2022), https://doi.org/10.1016/j.molstruc.2022.132751.

[14] C. Dlamini, V.M. Maphiri, L.T. Melato, T.P. Mokoena, M.R. Mhlongo, Tuneable blue-green co-activated CaAl2O4: 0.1 mol% Tb3+, x mol% Sm3+ (0 ≤ x ≤ 2) nanophosphor prepared by citrate sol-gel method, Opt. Mater. 142 (2023) 113985, https://doi.org/10.1016/J.OPTMAT.2023.113985.

[15] M.T. Tsai, Y.X. Chen, P.J. Tsai, Y.K. Wang, Photoluminescence of manganese-doped ZnAl2O4 nanophosphors, Thin Solid Films 518 (2010) e9, https://doi.org/10.1016/j.tsf.2010.03.130.

[16] M. Gao, J. Yang, L. Yang, Y. Zhang, J. Lang, H. Liu, H. Fan, Y. Sun, Z. Zhang, H. Song, Enhancement of optical properties and donor-related emissions in Y-doped ZnO, Superlattice. Microst. 52 (2012) 84–91, https://doi.org/10.1016/j.spmi.2012.03.016.

[17] S. Anandan, S. Muthukumaran, Influence of Yttrium on optical, structural and photoluminescence properties of ZnO nanopowders by sol-gel method, Opt. Mater. 35 (2013) 2241–2249, https://doi.org/10.1016/j.optmat.2013.06.009.

[18] R. Viswanath, H.S.B. Naik, Y.K.G. Somalanaik, P.K.P. Neelanjeneallu, K.N. Harish, M.C. Prabhakara, Studies on characterization, optical absorption, and photoluminescence of yttrium doped ZnS nanoparticles, J Nanotechnol 2014 (2014), https://doi.org/10.1155/2014/924797.

[19] X. Gao, J. Bi, L. Xie, C. Liu, J. Rong, C. Che, S. Leung, Preparation of NiFe2O4@ slit modified hollow carbon fiber via electrospinning for supercapacitor electrode material, J. Power Sources 591 (2024), https://doi.org/10.1016/j.jpowsour.2023.233838.

[20] C. Lai, Y. Wang, L. Fu, H. Song, B. Liu, D. Pan, Z. Guo, I. Seok, K. Li, H. Zhang, M. Dong, Aqueous flexible all-solid-state NiCo-Zn batteries with high capacity based on advanced ion-buffering reservoirs of NiCo 2 O 4, (n.d.). https://doi.org/10.1007/s42114-021-00375-1.

[21] G. Rutavi, D.J. Tarimo, V.M. Maphiri, M. Ncholu, Two-step Electrodeposition of Hausmannite Sulphur Reduced Graphene Oxide and Cobalt-Nickel Layered Double Hydroxide Heterostructure for High-Performance Supercapacitor, 2022, pp. 1–14, https://doi.org/10.1002/er.7922.

[22] B.M. Chong, N.H.N. Azman, M.A.A.M. Abdah, Y. Sulaiman, Supercapacitive performance of N-doped graphene/Mn 3 O 4/Fe 3 O 4 as an electrode material, Appl. Sci. 9 (2019), https://doi.org/10.3390/app9061040.

[23] S. Adewinbi, V. Maphiri, R. Marnadu, M. Shkir, N.M.H. Alsdran, H. Algarni, G. Sujithkumar, B. Taleatu, T. Niyitanga, H. Kim, Transparent, photosensitive and highly efficient pseudocapacitive binder-free Mo-modified NiO thin film electrode for bifunctional optoelectronic and energy storage applications, J. Alloys Compd. 937 (2023), https://doi.org/10.1016/j.jallcom.2022.168304.

[24] S. Sarr, N.F. Sylla, D.T. Bakhoum, N.M. Ndiaye, D.J. Tarimo, V.M. Maphiri, B.D. Ngom, N. Manyala, Vanadium dioxide sulphur-doped reduced graphene oxide composite as novel electrode material for electrochemical capacitor, J. Energy Storage 55 (2022), https://doi.org/10.1016/j.est.2022.105666.

[25] S.A. Adewinbi, B.A. Taleatu, V.M. Maphiri, O. Fasakin, E. Omotoso, K.O. Oyedotun, N. Manyala, Characterization of two-way fabricated hybrid metal-oxide nanostructured electrode materials for photovoltaic and miniaturized supercapacitor applications, Solid State Sci. 119 (2021), https://doi.org/10.1016/j.solidstatesciences.2021.106699.

[26] S.A. Adewinbi, V.M. Maphiri, B.A. Taleatu, R. Marnadu, M. Shkir, J. Hakami, W.K. Kim, S. Gedi, Binder-less fabrication, some surface studies, and enhanced electrochemical performance of Co, Cu-embedded MnO2 thin film electrodes for supercapacitor application, Ceram. Int. 48 (2022) 26312–26325, https://doi.org/10.1016/j.ceramint.2022.05.315.

[27] X. Xu, J. Li, A. Dymerska, J.J. Koh, J. Min, S. Liu, J. Azadmanjiri, E. Mijowska, MIL-53(Al) assisted in upcycling plastic bottle waste into nitrogen-doped hierarchical porous carbon for high-performance supercapacitors, Chemosphere 340 (2023), https://doi.org/10.1016/j.chemosphere.2023.139865.

[28] S. Remesh, M. Vasudevan, M. Sivakumar, V. Perumal, M. Ovinis, S. Karuppanan, T.N.J.I. Edison, P.B. Raja, M.N.M. Ibrahim, A.F.B.A. Latip, N. Arumugam, R. S. Kumar, In-situ Mg-Al LDH infused lignin-derived laser scribed graphene for facilitated ion transport in flexible supercapacitor application, J. Taiwan Inst. Chem. Eng. 153 (2023), https://doi.org/10.1016/j.jtice.2023.105247.

[29] E.S. Goda, S.E. Hong, B. Pandit, A. ur Rehman, B.S. Singu, M.S. Akhtar, M. Sohail, S.M. El-Bahy, H. Gamal, K.R. Yoon, Metal-organic framework (MOF) templated hierarchical Al-doped CoxP @ graphene composite: a promising solid-state asymmetric supercapacitor with PANI derived carbon nanorods, J. Alloys Compd. 965 (2023), https://doi.org/10.1016/j.jallcom.2023.171183.

[30] A. Bele, M.R. Mhlongo, L.F. Koao, T.E. Motaung, T.D. Malevu, T.T. Hlatshwayo, S. Mpelane, M. Mlambo, S.V. Motloung, Effects of varying Sm3+ concentration on the structure, morphology and photoluminescence properties of the BaAl2O4/CaAl2O4/Ca4Al6O13/Ca3Al2O6:x% Sm3+ (0 ≤ x ≤ 1.9) mixed phases using citrate sol-gel method, Heliyon 8 (2022) e12573, https://doi.org/10.1016/j.heliyon.2022.e12573.

[31] V.M. Maphiri, J. Wesley-Smith, S.V. Motloung, Phase transition and optical properties of Ba1-xZnxAl2O4:0.1% Eu3+ prepared via citrate sol-gel method, J. Lumin. 215 (2019), https://doi.org/10.1016/j.jlumin.2019.116710.

[32] S. Iaiche, A. Djelloul, ZnO/ZnAl2O4 nanocomposite films studied by X-Ray diffraction, FTIR, and X-Ray photoelectron spectroscopy, Journal of Spectroscopy 2015 (2015), https://doi.org/10.1155/2015/836859.

[33] T.S. Mabelane, L.F. Koao, S.V. Motloung, T.E. Motaung, R.E. Kroon, M.R. Mhlongo, Effect of annealing period on the structure, morphology, and optical properties of CaAl2O4:0.1% Sm3+ prepared by citrate sol-gel method, J. Mol. Struct. 1260 (2022) 132751, https://doi.org/10.1016/j.molstruc.2022.132751.

[34] C. Dlamini, V.M. Maphiri, L.T. Melato, T.P. Mokoena, M.R. Mhlongo, Tuneable blue-green co-activated CaAl2O4: 0.1 mol% Tb3+, x mol% Sm3+ (0 ≤ x ≤ 2) nanophosphor prepared by citrate sol-gel method, Opt. Mater. 142 (2023) 113985, https://doi.org/10.1016/j.optmat.2023.113985.

[35] B.S. Shashikala, H.B. Premkumar, G.P. Darshan, H. Nagabhushana, S.C. Sharma, S.C. Prashantha, H.P. Nagaswarupa, Synthesis and photoluminescence studies of an orange red color emitting novel CaAl2O4: Sm3+ nanophosphor for LED applications, Mater. Today Proc. 4 (2017) 11820–11826, https://doi.org/10.1016/j.matpr.2017.09.100.

[36] V. Mote, Y. Purushotham, B. Dole, Williamson-Hall analysis in estimation of lattice strain in nanometer-sized ZnO particles, Journal of Theoretical and Applied Physics 6 (2012) 2–9, https://doi.org/10.1186/2251-7235-6-6.

[37] H.R. An, S.H. Baek, I.K. Park, H.J. Ahn, Electrical and optical properties of Al-doped ZnO films deposited by atomic layer deposition, Korean Journal of Materials Research 23 (2013) 469–475, https://doi.org/10.3740/MRSK.2013.23.8.469.

[38] H. Nayebzadeh, N. Saghatoleslami, M. Tabasizadeh, Optimization of the activity of KOH/calcium aluminate nanocatalyst for biodiesel production using response surface methodology, J. Taiwan Inst. Chem. Eng. 68 (2016) 379–386, https://doi.org/10.1016/j.jtice.2016.09.041.

[39] S.P. Khambule, S.V. Motloung, T.E. Motaung, L.F. Koao, R.E. Kroon, M.A. Malimabe, Tuneable blue to orange phosphor from Sm3+ doped ZnAl2O4 nanomaterials, Results in Optics 9 (2022) 100280, https://doi.org/10.1016/j.rio.2022.100280.

[40] M.Y. Nassar, I.S. Ahmed, I. Samir, A novel synthetic route for magnesium aluminate (MgAl2O 4) nanoparticles using sol-gel auto combustion method and their photocatalytic properties, Spectrochim. Acta Mol. Biomol. Spectrosc. 131 (2014) 329–334, https://doi.org/10.1016/j.saa.2014.04.040.

[41] J. Yang, R. Wang, L. Yang, J. Lang, M. Wei, M. Gao, X. Liu, J. Cao, X. Li, N. Yang, Tunable deep-level emission in ZnO nanoparticles via yttrium doping, J. Alloys Compd. 509 (2011) 3606–3612, https://doi.org/10.1016/j.jallcom.2010.12.102.

[42] A.A. Shoustikov, Y. You, M.E. Thompson, Electroluminescence color tuning by dye doping in organic light-emitting diodes, IEEE J. Sel. Top. Quant. Electron. 4 (1998) 3–13, https://doi.org/10.1109/2944.669454.

[43] C.S. McCamy, Correlated color temperature as an explicit function of chromaticity coordinates, Color Res. Appl. 17 (1992) 142–144, https://doi.org/10.1002/col.5080170211.

[44] M.A. Rodríguez, C.L. Aguilar, M.A. Aghayan, Solution combustion synthesis and sintering behavior of CaAl 2O4, Ceram. Int. 38 (2012) 395–399, https://doi.org/10.1016/j.ceramint.2011.07.020.

[45] M.M. Rahman, M. Muttakin, A. Pal, A.Z. Shafiullah, B.B. Saha, A statistical approach to determine optimal models for IUPAC-classified adsorption isotherms, Energies 12 (2019), https://doi.org/10.3390/en12234565.

[46] Y. He, J. Pan, L. Wu, Y. Zhu, X. Ge, J. Ran, Z.J. Yang, T. Xu, A novel methodology to synthesize highly conductive anion exchange membranes, Sci. Rep. 5 (2015) 1–7, https://doi.org/10.1038/srep13417.

[47] M.N. Rantho, M.J. Madito, N. Manyala, Symmetric supercapacitor with supercapattery behavior based on carbonized iron cations adsorbed onto polyaniline, Electrochim. Acta 262 (2018) 82–96, https://doi.org/10.1016/j.electacta.2018.01.001.

[48] M.N. Rantho, M.J. Madito, N. Manyala, High-performance symmetric supercapacitor device based on carbonized iron-polyaniline/nickel graphene foam, J. Alloys Compd. 819 (2020) 152993, https://doi.org/10.1016/j.jallcom.2019.152993.

[49] D.J. Tarimo, K.O. Oyedotun, A.A. Mirghni, N. Manyala, Sulphur-reduced graphene oxide composite with improved electrochemical performance for supercapacitor applications, Int. J. Hydrogen Energy 45 (2020) 13189–13201, https://doi.org/10.1016/j.ijhydene.2020.03.059.

[50] T.S. Mathis, N. Kurra, X. Wang, D. Pinto, P. Simon, Y. Gogotsi, Energy storage data reporting in perspective—guidelines for interpreting the performance of electrochemical energy storage systems, Adv. Energy Mater. 9 (2019) 1–13, https://doi.org/10.1002/aenm.201902007.

[51] N.F. Sylla, N.M. Ndiaye, B.D. Ngom, D. Momodu, M.J. Madito, B.K. Mutuma, N. Manyala, Effect of porosity enhancing agents on the electrochemical performance of high-energy ultracapacitor electrodes derived from peanut shell waste, Sci. Rep. 9 (2019) 1–15, https://doi.org/10.1038/s41598-019-50189-x.

[52] A. Moyseowicz, Z. González, R. Menéndez, G. Gryglewicz, Three-dimensional poly(aniline-co-pyrrole)/thermally reduced graphene oxide composite as a binder-free electrode for high-performance supercapacitors, Compos. B Eng. 145 (2018) 232–239, https://doi.org/10.1016/j.compositesb.2018.03.018.

[53] B. Zhao, P. Liu, Y. Jiang, D. Pan, H. Tao, J. Song, T. Fang, W. Xu, Supercapacitor performances of thermally reduced graphene oxide, J. Power Sources 198 (2012) 423–427, https://doi.org/10.1016/j.jpowsour.2011.09.074.

[54] V.M. Maphiri, D.T. Bakhoum, S. Sarr, N.F. Sylla, G. Rutavi, N. Manyala, Impact of thermally reducing temperature on graphene oxide thin films and microsupercapacitor performance, Nanomaterials 12 (2022), https://doi.org/10.3390/nano12132211.

[55] M. Mahdavian, M.M. Attar, Another approach in analysis of paint coatings with EIS measurement: phase angle at high frequencies, Corros Sci 48 (2006) 4152–4157, https://doi.org/10.1016/j.corsci.2006.03.012.